



Effects of Acetylene Flow Rate on Structure, Mechanical Properties, and Tribological Properties of Cr-CH_x Coatings Deposited by Radio Frequency Magnetron Sputtering

Y.L. Su, W.H. Kao, and G.Y. Chen

Submitted: 5 April 2021 / Revised: 11 June 2021 / Accepted: 30 June 2021 / Published online: 4 August 2021

Cr-CH_x coatings (where x indicates the acetylene flow rate and has a value in the range of 5 to 35 sccm) were deposited on high-speed steel substrates using a radio frequency magnetron sputtering system. The crystalline phases of the deposited coatings were characterized using x-ray diffraction. The surface morphologies and cross-sectional microstructures were analyzed using scanning electron microscopy. The XRD results showed that the coatings consisted mainly of Cr₇C₃ and metal Cr crystalline phases. In addition, the Raman spectra analysis results showed that the Cr-CH₂₅ and Cr-CH₃₅ coatings had I_D-I_G ratios of 1.08 and 1.22, respectively. The coating hardness gradually decreased with an increasing acetylene flow rate. By contrast, the adhesion strength increased as the flow rate increased beyond 15 sccm. Among all the coatings, the Cr-CH₃₅ coating showed the best tribological properties, with an average friction coefficient of 0.048 and wear rate of 0.28×10⁻⁶ mm³/Nm under a load of 8 N.

Keywords adhesion, coating, Cr-CH, tribological property

1. Introduction

The machining of high-precision, high-quality products demands the use of machine tools with a high strength and good stability. Many studies have demonstrated the effectiveness of surface coating technologies in improving the mechanical and tribological properties of machine tool materials (Ref 1-3). Among the many different coating materials available, chromium-based coatings such as CrC-SiC and CrC are particularly suitable for the protection of machine components or sliding bearing applications due to their high wear resistance, good anti-corrosion performance, high oxidation resistance, and superior hardness (Ref 4, 5). Chromium carbides have various crystallographic structures, including orthorhombic Cr₃C₂, hexagonal Cr₇C₃ and cubic Cr₂₃C₆, depending on the reaction temperature and gas composition (Ref 6, 7). Crystalline Cr₃C₂ yields the best mechanical properties (e.g., the highest hardness), and is thus one of the most commonly used protective coatings for industrial components and tools (Ref 8). However, hexagonal Cr₇C₃ has a higher binding energy than Cr₃C₂ or Cr₂₃C₆ (Ref 9). Thus, it is also a suitable coating material for high-speed steel or tungsten carbide substrates (Ref 10-12).

Chromium carbide coatings are usually deposited using physical vapor deposition (PVD) methods due to the ability they provide to obtain high-density and chemically pure coatings under low temperatures (Ref 13-17). While many

PVD techniques are available, including radio frequency (RF), direct current (DC) and high-power impulse magnetron sputtering (HiPIMS) (Ref 18), RF sputtering has many practical advantages, including a higher deposition rate, an improved homogeneity of the deposited coating, and a superior adhesion strength (Ref 19-23). Accordingly, in the present study, Cr-CH_x coatings (where x is the acetylene flow rate and varies in the range of 5 to 35 sccm) are deposited on high-speed steel (SKH51) substrates using an unbalanced RF magnetron sputtering system. The effects of the acetylene flow rate on the composition, structure, mechanical performance, and tribological properties of the Cr-CH_x coatings are then systematically explored.

2. Experimental

2.1 Sample Preparation

Cr-CH_x coatings were deposited on SKH51 substrates and Si (100) wafers. The SKH51 substrates (diameter: 24 mm; thickness: 8 mm) were polished to a final roughness of Ra=8 nm prior to the deposition process and were used to evaluate the mechanical and tribological properties of the various coatings. Meanwhile, the silicon wafers were used to examine the crystalline structures and chemical compositions of the different coatings.

2.2 Coating Deposition Process

The substrates were sputter-cleaned for 20 min using Ar ions and a substrate bias voltage of -280 V prior to the deposition process in order to improve the adhesion between the subsequent coatings and the substrate. The coatings were deposited using a radio frequency unbalanced magnetron sputtering system (Teer-450C, Teer Coating, United Kingdom) with a hybrid C₂H₂/Ar mixture as the reactant gas. As shown in Fig. 1, the deposition process was performed using four

Y.L. Su and G.Y. Chen, Department of Mechanical Engineering, National Cheng Kung University, Tainan, Taiwan; and W.H. Kao, Department of Automation Engineering & Institute of Mechatronic Systems, Chienkuo Technology University, Changhua, Taiwan. Contact e-mail: n18851158@yahoo.com.tw.

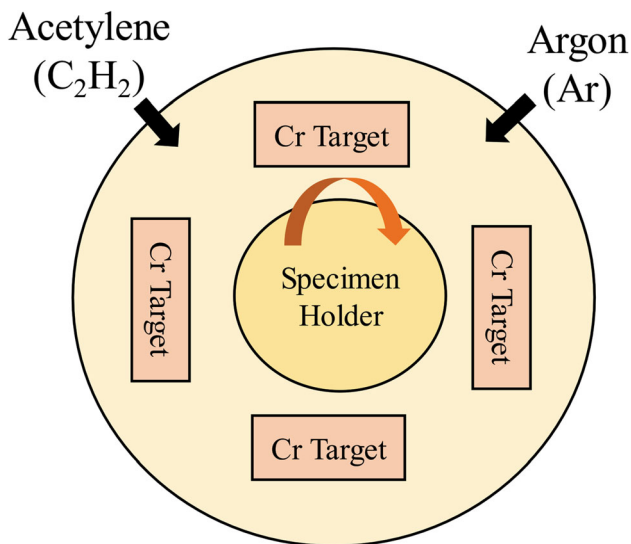


Fig. 1 Schematic illustration of sputtering arrangement

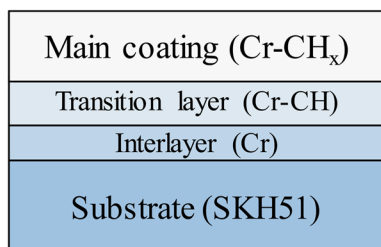


Fig. 2 Schematic illustration showing multi-layer structure of Cr-CH_x coatings

chromium targets (99.9% purity) uniformly arranged around the sample. To improve the uniformity of the coatings, the substrate was rotated at a constant speed of 1 rpm throughout the deposition process. Each coating consisted of a Cr interlayer, a Cr-CH transitional layer, and the main Cr-CH_x coating, as shown in Fig. 2. The interlayer and transitional layer both served to enhance the adhesion between the main coating (Cr-CH_x) and the substrate.

The sputtering parameters used to prepare the various Cr-CH_x coatings are shown in Table 1. Taking the Cr-CH₅ coating for illustration purposes, the Cr interlayer was sputtered using a target current of 1.5 A and a deposition time of 5 min. Once the interlayer had been deposited, the target current was increased to 2.5 A and the acetylene flow rate was gradually increased from 0 to 5 sccm over a period of 10 min to form the Cr-CH transitional layer. Finally, the target current was maintained at 2.5 A and the main Cr-CH₅ coating layer was sputtered with a fixed acetylene flux of 5 sccm and a deposition time of 25 min. Cr-CH_x coatings were prepared using various acetylene fluxes in the range of 5 to 35 sccm using a constant target current of 2.5 A, an Ar gas flow rate of 20 sccm and a substrate bias voltage of -60 V. It was reported in (Ref 24) that an excessive carbon content may cause target poisoning. Furthermore, the preliminary results obtained in the present study also showed that severe target poisoning occurred at an acetylene flux of 40 sccm. Accordingly, in the present experiments, the maximum acetylene flux was deliberately limited to 35 sccm.

2.3 Coating Characterization

The microstructures and elemental compositions of the various coatings were characterized by a field emission scanning electron microscope (SU-5000, HITACHI Japan) integrated with energy-dispersive x-ray spectroscopy (EDS). The crystallographic structures of the coatings were analyzed using an x-ray diffractometer (D/MAX 2500, Rigaku, Japan) with Cu-K α radiation at 40 kV and 100 mA. The chemical bonding was analyzed using x-ray photoelectron spectroscopy (XPS) with a light source of Al K α , operating at a wavelength of 100 μ m and the bounding energy was scanned in the range of 0-1400 eV. The Gaussian-Lorentzian method was used to calculate the XPS spectrum. The results of XPS are fitted by OriginLab software (OriginLab Corporation, Massachusetts, USA) in order to obtain the chemical bonding ratio for coatings. The carbon bonds in the various coatings were analyzed using a Raman spectrometer (RM1000, Renishaw, England) with a central bandwidth of 633 nm. The adhesive properties were evaluated using a scratch tester (FM-POD-200NT, Freeform, Taiwan) fitted with a diamond tip with a diameter of 0.3 mm under a gradually increasing load of 0-100 N (rate: 10 N/mm, increment 1 N every second). Finally, the hardness and elastic modulus properties of the coatings were measured using a nanoindenter (LBI nanoindenter, UNAT-M, BMT, Germany) under a maximum indentation load of 10 mN.

2.4 Tribological Tests

The tribological properties of the various coatings were evaluated using a ball-on-disk wear system (FM-POD-200NT, Freeform, Taiwan) with a \varnothing 3/32-inch Si₃N₄ ball as the counterbody. The tests were performed under normal loads of 2, 5 and 8 N, respectively, with a sliding diameter of 10 mm, a sliding speed of 200 mm/s, and a total sliding distance of 350 m (9284 rotations). Following the wear tests, the wear widths and wear depths of the coating surface were measured using a white light interferometer (Contour GT-K 3D, Bruker, USA). For each sample, the wear rate was calculated as $2\pi RA/(N \times m)$, where R is the radius of the wear track, A is the cross-sectional wear area, N is the normal load, and m is the total sliding distance. The wear tracks were also observed using SEM and analyzed using EDS to determine the elemental composition.

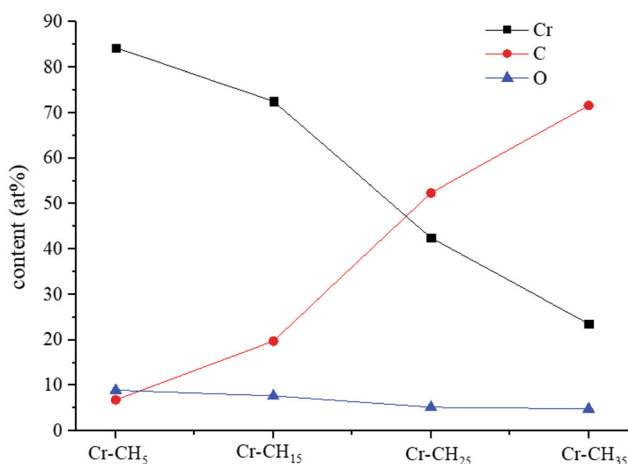
3. Results and Discussion

3.1 Coating Characteristics

Figure 3 shows the chemical compositions of the various Cr-CH_x coatings. It is seen that the carbon content of the coatings gradually increases from 6.8 to 71.6 at.% as the acetylene flux increases from 5 to 35 sccm. By contrast, the chromium content decreases from 84.3 to 23.6 at.%. All of the coatings contain a small amount of oxygen (4-8 at.%). It is speculated that this oxygen originates from either residual water vapor within the vacuum chamber, or the ambient environment on removal of the samples from the chamber. A detailed inspection of Fig. 3 shows that the Cr-CH₅ coating consists mainly of Cr (84.3 at.%) and a little C (6.8 at.%). By contrast, the Cr-CH₁₅ coating consists of 72.6 at.% Cr and 19.8 at.% C. When the C₂H₂ flux is increased to 25 sccm, the coating contains just 42.5 at.% Cr and 52.4 at.% C. In other words, the deposition efficiency of the

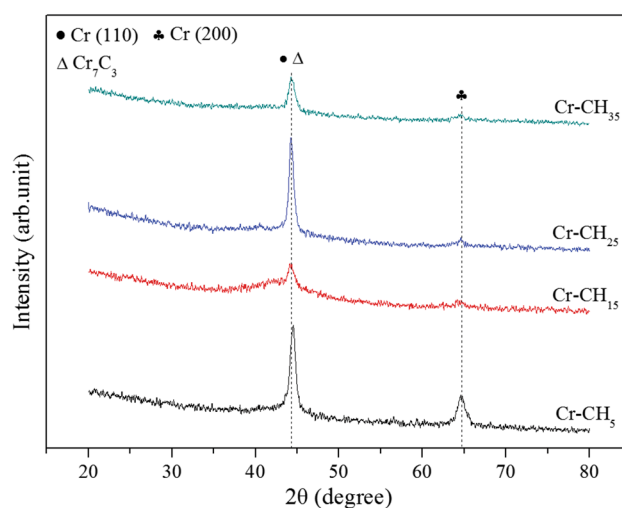
Table 1 Sputtering parameters used for deposition of Cr-CH_x coatings

Coating	Cr-CH ₅	Cr-CH ₁₅	Cr-CH ₂₅	Cr-CH ₃₅
Interlayer	Cr Target Current 1.5A			
Time: 5 min				
Transition layer	Cr Target Current 2.5A			
Time: 10 min				
Cr-CH _x Time: 25 min	C ₂ H ₂ 0~5 sccm	C ₂ H ₂ 0~15 sccm	C ₂ H ₂ 0~25 sccm	C ₂ H ₂ 0~35 sccm
	Cr Target Current 2.5A			
	C ₂ H ₂ 5 sccm	C ₂ H ₂ 15 sccm	C ₂ H ₂ 25 sccm	C ₂ H ₂ 35 sccm
Fixed parameters	Argon gas: 20 sccm			
	Substrate bias: -60V			
	Sputtering power: 900 W			
	RF frequency: 13.56 MHz			
	Rotation speed: 1 rpm			
	Base pressure: 2.67×10 ⁻³ Pa			
	Total time: 40 min			

**Fig. 3** Elemental compositions of Cr-CH_x coatings

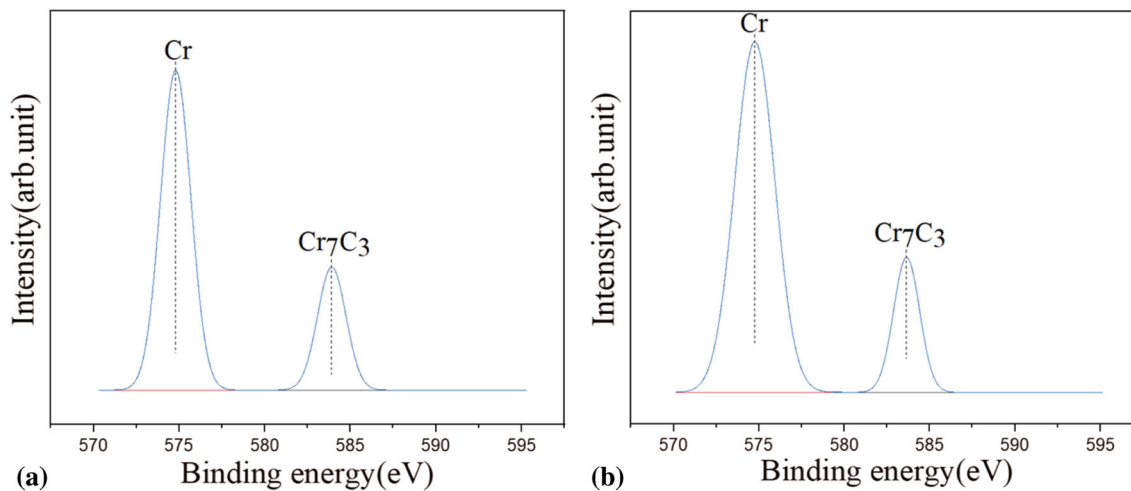
Cr targets decreases as the C₂H₂ flux is increased beyond 15 sccm. The target poisoning effect is particularly apparent at the highest C₂H₂ flux of 35 sccm, for which the coating (Cr-CH₃₅) contains just 23.6 at.% Cr and has a high C concentration of 71.6 at.%.

Figure 4 shows the XRD patterns of the various coatings. All of the patterns contain prominent peaks at $2\theta = 44.37^\circ$ and $2\theta = 64.63^\circ$, corresponding to Cr₇C₃ (or Cr (110)) and Cr (200) crystalline phases, respectively. However, none of the patterns contain carbon diffraction peaks. Thus, it is inferred that the coatings have an amorphous structure (Ref 25). It is seen that the peak intensities in the Cr-CH₅ coating pattern are higher than those in any of the other patterns. In other words, the coating consists mainly of pure Cr and contains only a small amount of C. Interestingly, the peaks in the XRD pattern of the Cr-CH₁₅ coating have a lower intensity than those in any of the other patterns. Moreover, the peak at $2\theta = 44.37^\circ$ is particularly low and broad. Hence, it is inferred that the Cr-CH₁₅ coating has a transition phase between Cr crystalline phase and Cr₇C₃ phase, respectively, and possesses both Cr (110) and Cr₇C₃ as a result (Ref 26). For the Cr-CH₂₅ and Cr-CH₃₅ coatings, the main peaks correspond to Cr₇C₃ phase and the Cr (200) peak intensity reduces due to the higher carbon content. However, as

**Fig. 4** XRD patterns of Cr-CH_x coatings

the carbon content increases, the intensity of the Cr₇C₃ peak reduces and the coating approaches an amorphous phase structure. According to (Ref 27-29), the short-range coordination in Cr-rich phase is similar to that of hexagonal Cr₇C₃. For carbon contents greater than 30 at.%, CrC coatings contain abundant Cr₇C₃ phase, and the excess carbon atoms assemble in the form of amorphous carbon phase (Ref 28, 29). Thus, as shown in Fig. 4, the XRD patterns of the Cr-CH₂₅ and Cr-CH₃₅ coatings contain dominant Cr₇C₃ peaks, while the intensities of the Cr (200) peaks reduce. Notably, the peak intensity of the Cr-CH₃₅ coating is slightly lower than that of the Cr-CH₂₅ coating, which suggests that as the carbon content increases, the formation of Cr₇C₃ phase weakens and the coating approaches an amorphous phase. In addition, Fig. 5(a) and (b) shows the XPS spectra and peak fitting results of the Cr-CH₂₅ and Cr-CH₃₅ coatings, respectively. As shown in Fig. 5(a) and (b), the Cr₇C₃ binding percentage of Cr-CH₃₅ (20%) is lower than Cr-CH₂₅ (26.5%). This result is as mentioned above, the increase in carbon content weakens the Cr₇C₃ phase.

Figure 6(a) and (b) shows the Raman spectra of the Cr-CH₂₅ and Cr-CH₃₅ coatings, respectively. (Note that the Cr-CH₅ and Cr-CH₁₅ coatings showed no obvious Raman characteristic



Coating	Binding percentage (%)	
	Cr	Cr ₇ C ₃
Cr-CH ₂₅	73.5	26.5
Cr-CH ₃₅	80	20

Fig. 5 High-resolution XPS spectra and peak fitting results for (a) Cr-CH₂₅ and (b) Cr-CH₃₅ coatings in Cr 2p region

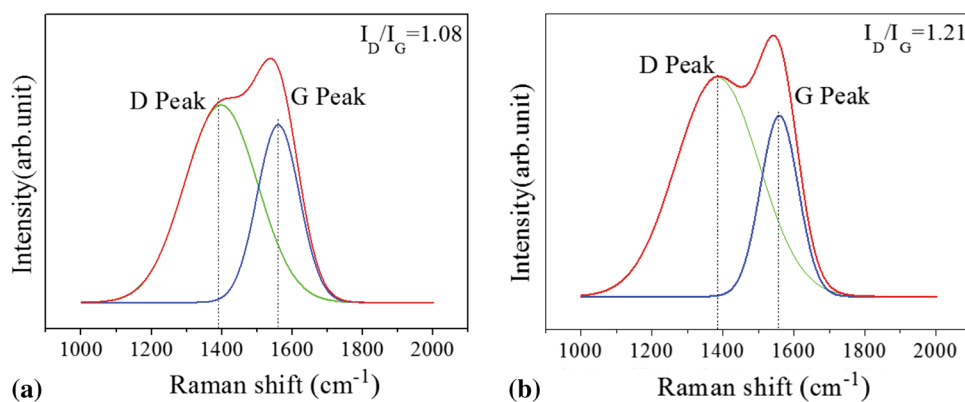


Fig. 6 Raman spectra of (a) Cr-CH₂₅ and (b) Cr-CH₃₅ coatings showing I_D-I_G values calculated using fitting results for peak heights

peaks and hence the corresponding spectra are deliberately omitted here.) The spectra indicate that both coatings have a characteristic amorphous diamond-like carbon (DLC) structure (Ref 30). For the Cr-CH₂₅ coating, the D and G peaks are located at 1391 and 1557 cm⁻¹, respectively. By contrast, for the Cr-CH₃₅ coating, the two peaks shift to 1384 and 1559 cm⁻¹, respectively. In general, the existence of the D and G peaks in Raman spectra depends directly on the ordering of the sp² sites and indirectly on the fraction of sp³ sites (Ref 30, 31). Moreover, the relative intensity ratio of the two peaks (i.e., I_D/I_G) can be used to characterize the sp²/sp³ ratio of the structure (Ref 32, 33). In particular, a higher I_D-I_G value indicates a higher ratio of sp² bonds to sp³ bonds (Ref 34, 35). According to the fitting results for the present Raman spectra, the Cr-CH₂₅ and Cr-CH₃₅ coatings have I_D-I_G ratios of 1.08 and 1.21,

respectively. In other words, the Cr-CH₃₅ coating has a higher fraction of sp² bonds than the Cr-CH₂₅ coating.

Figure 7 presents SEM cross-sectional micrographs of the various Cr-CH_x coatings. As shown in Fig. 7(a), (b) and (c), the Cr-CH₅, Cr-CH₁₅ and Cr-CH₂₅ coatings all have a columnar structure. However, the structure of the Cr-CH₁₅ coating is obviously less dense than that of the Cr-CH₅ and Cr-CH₂₅ coatings. Moreover, as the C₂H₂ flux is increased to 35 sccm, the coating transforms to a featureless structure, as shown in Fig. 7(d). Figure 8 shows the thickness of the four Cr-CH_x coatings. From inspection, the Cr-CH₅, Cr-CH₁₅, Cr-CH₂₅ and Cr-CH₃₅ coatings have thicknesses of 2.16, 1.77, 1.60 and 1.84 μm, respectively. In other words, the coating thickness first decreases and then increases as the C₂H₂ flux is increased. The gradual reduction in the coating thickness as the flux increases from 5 to 25 sccm can be attributed to the target poisoning

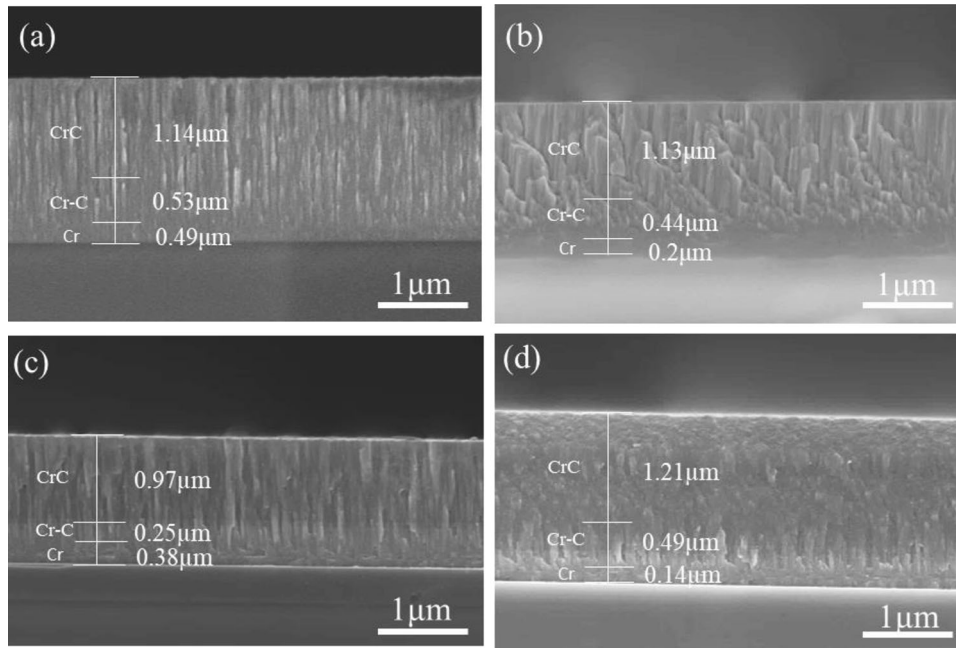


Fig. 7 SEM cross-sectional micrographs of (a) Cr-CH₅, (b) Cr-CH₁₅, (c) Cr-CH₂₅ and (d) Cr-CH₃₅ coatings

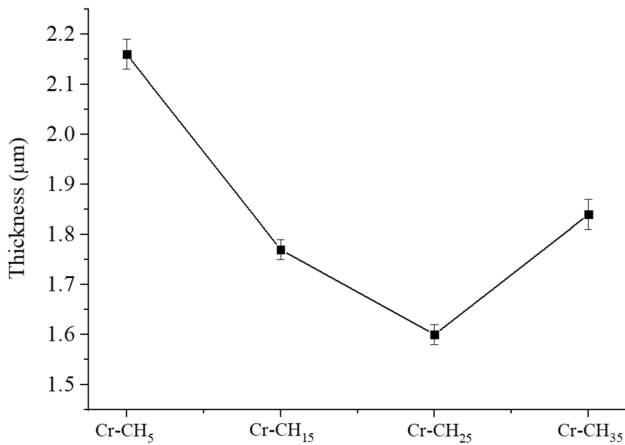


Fig. 8 Thickness of Cr-CH_x coatings

effect. However, as the C₂H₂ flux is further increased to 35 sccm, the Ar partial pressure reduces, and hence the number of collisions between the Ar ions and the metal particles in the chamber also reduces (Ref 36). As a result, a greater number of Cr atoms are incident on the substrate, and hence the deposition rate increases.

3.2 Mechanical Properties

Table 2 shows the mechanical properties of the various coatings. It is seen that the hardness (H) and elastic modulus (E) gradually decrease as the acetylene flow rate increases from 5 to 35 sccm. The Cr-CH₅ coating thus has the highest hardness of the different coatings (26.2 GPa), while the Cr-CH₃₅ coating has the lowest (15.2 GPa). The reduction in hardness with an increasing acetylene flux can be attributed to the higher carbon content. It is noted that this inference is consistent with the findings of Su et al. and Jhong et al. (Ref 37, 38) that the

Table 2 Mechanical properties of Cr-CH_x coatings

Coating	Hardness, GPa	Elastic modulus, GPa	H/E	Adhesion strength, Lc, N
Cr-CH ₅	26.2±1.78	505.1±9.45	0.052	12±1.85
Cr-CH ₁₅	22.4±0.9	392.8±23.05	0.057	> 100
Cr-CH ₂₅	17.4±1.47	277.6±18.93	0.063	> 100
Cr-CH ₃₅	15.2±1.46	182±3.96	0.084	> 100

hardness of thin-film coating systems decreases with an increasing carbon content. The high hardness of the present Cr-CH₅ coating (26.2 GPa) can be attributed to the atomic size mismatch between the chromium and carbon atoms (i.e., 128 and 70 pm, respectively), which leads to a dislocation induced solid solution strengthening effect. According to (Ref 39), Cr₇C₃ phase has a relatively low hardness of 15.7 GPa. Thus, for the present coatings with a higher carbon content, e.g., the Cr-CH₂₅ and Cr-CH₃₅ coatings with a DLC structure, an increased number of sp² bonds, the coating hardness are significantly reduced. By contrast, the H/E ratio of the Cr-CH_x coatings increases from 0.052 to 0.084 as the acetylene flux is increased from 5 to 35 sccm. It has been reported that a higher H/E ratio is associated with a greater wear resistance since the coating is able to absorb a greater amount of energy prior to destruction (Ref 40, 41). Thus, the results in Table 2 suggest that the Cr-CH₃₅ coating, with the highest H/E ratio of the present coatings, has the optimum tribological properties (see also sect. 3.3).

In the scratch tests, the critical load (L_c) was defined as the load at which the coating within the scratch track was completely destroyed. As shown in Table 2, the Cr-CH₅ coating has the lowest adhesion strength of all the coatings, with a critical load of just 12 N. However, for acetylene fluxes of 15 sccm or more, the critical load increases to more than 100 N; indicating that all of the coatings have a high adhesion strength. The Cr-CH₅, CH₁₅, CH₂₅ and CH₃₅ coatings showed average friction coefficients of 0.309, 0.269, 0.188 and 0.119, respectively, in the scratch tests. In other words, the friction coefficient significantly reduced with an increasing acetylene flux. It is speculated that this is the result of the formation of a solid lubricant layer at the sliding interface due to the higher carbon content of the coatings. This lubricant layer reduces the lateral force acting on the coating as the diamond tip is dragged across the surface and improves the adhesion strength accordingly. As shown in the SEM image in Fig. 9(a), the Cr-CH₅ coating ($L_c=12$ N) has significant spalling and is completely destroyed in the early stages of the scratch test. By contrast, the

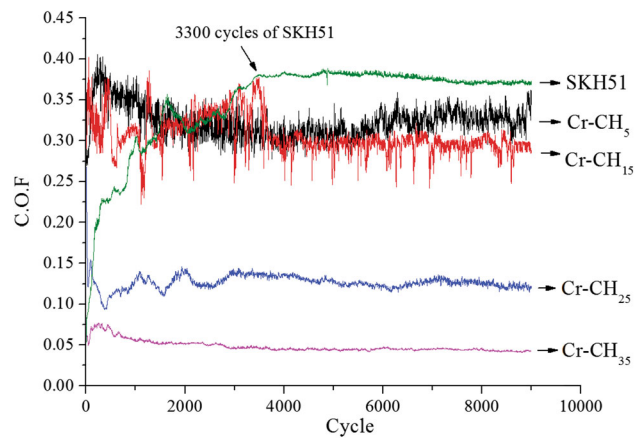


Fig. 10 Coefficients of friction of Cr-CH_x coatings and substrate under 8 N load

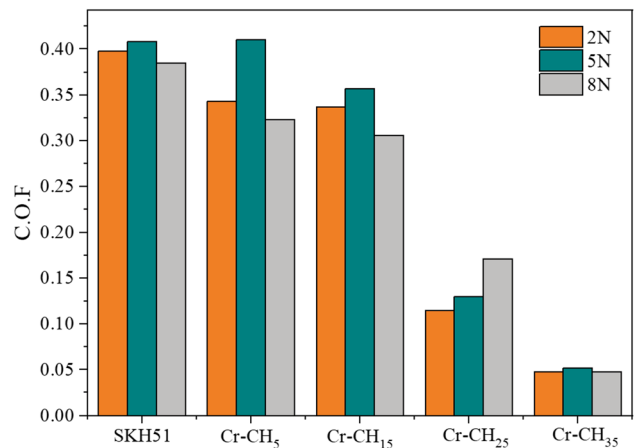


Fig. 11 Average friction coefficients of Cr-CH_x coatings and substrate

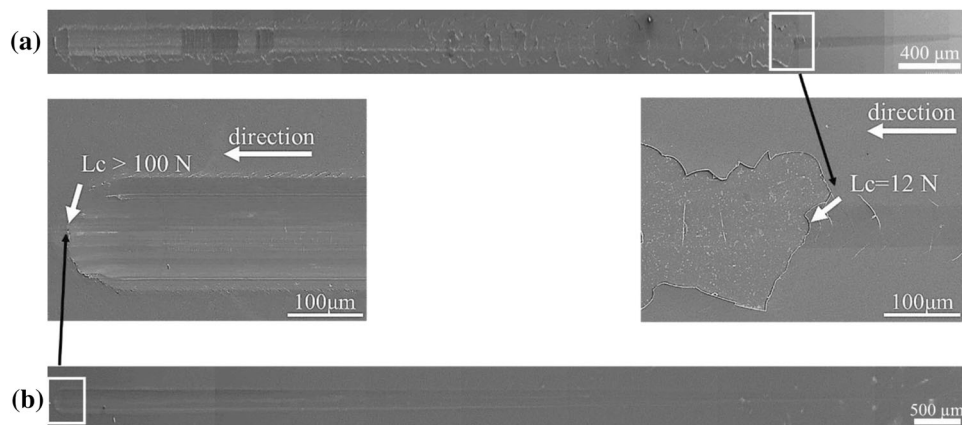


Fig. 9 SEM images of scratch tracks on (a) Cr-CH₅ and (b) Cr-CH₃₅ coatings

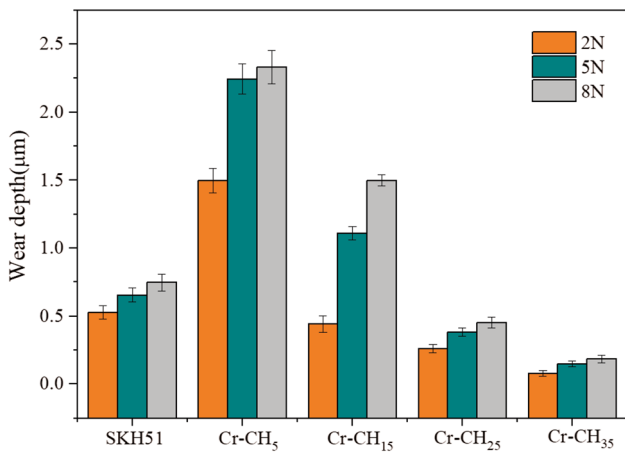


Fig. 12 Wear depths of Cr-CH_x coatings and substrate

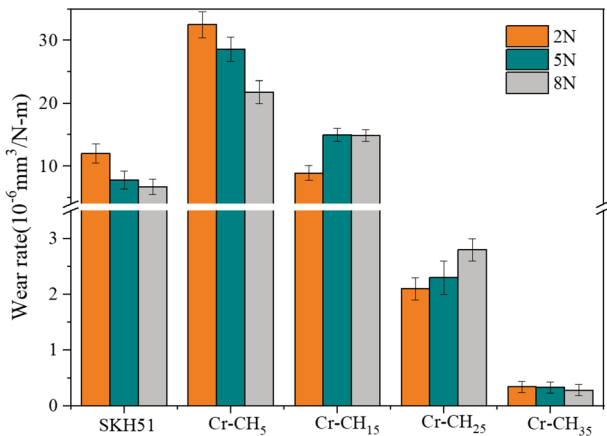


Fig. 13 Wear rates of Cr-CH_x coatings and substrate

Cr-CH₃₅ coating ($L_c = > 100$ N) shows evidence of only minor abrasion scars, even on completion of the scratch test (see Fig. 9b).

3.3 Tribological Properties

3.3.1 Friction Coefficient, Wear Depth and Wear Rate. Figure 10 shows the friction coefficient traces of the uncoated and coated substrates over the course of the sliding wear tests performed under a normal load of 8 N. (Note that similar friction coefficient traces were obtained under lower normal loads of 2 N and 5 N, respectively, and hence they are deliberately omitted here for reasons of conciseness.) For the uncoated SKH51 substrate, the friction coefficient increases rapidly for the first 3300 cycles and then remains approximately constant until the end of the test. For all of the coated samples, the friction coefficient is lower than that of the uncoated substrate. Furthermore, the friction coefficient reduces and becomes more stable as the acetylene flux increases.

Figure 11, 12 and 13 show the average friction coefficients, wear depths and wear rates of the various uncoated and coated samples under normal sliding loads of 2, 5 and 8 N, respectively. As shown in Fig. 11, the friction coefficients of the Cr-CH₅ and Cr-CH₁₅ coatings, with low carbon contents of 6.8 at.% and 19.8 at.%, respectively (see Fig. 3), are almost as high as those of the SKH51 substrate under all three normal

loads. However, for the Cr-CH₂₅ and Cr-CH₃₅ coatings, with high carbon contents of 52.4 at.% and 71.6 at.%, respectively, the friction coefficients are significantly reduced. Among all of the coatings, the Cr-CH₃₅ coating, with the highest carbon content (71.6 at.%), exhibits both the lowest friction coefficient (see Fig. 11) and the most stable friction coefficient (see Fig. 10). Referring to Fig. 12, it is seen that the wear depths of the Cr-CH₅ and Cr-CH₁₅ coatings are much higher than that of the uncoated substrate. Moreover, for both coatings, the wear depth increases significantly with an increasing load. However, for all values of the applied load, the wear depth gradually reduces as the C₂H₂ flow rate is increased beyond 15 sccm. For both the Cr-CH₂₅ coating and the Cr-CH₃₅ coating, the wear depth is noticeably lower than that of the SKH51 substrate. It is seen in Fig. 13 that the Cr-CH₅ and Cr-CH₁₅ coatings, with low carbon contents, have a higher wear rate than the SKH51 substrate. However, for the Cr-CH₂₅ and Cr-CH₃₅ coatings, the wear rate is significantly reduced.

Overall, the results presented in Fig. 12 and 13 show that the Cr-CH₅ coating has the highest wear depth and wear rate of all the coatings. The poor tribological properties of the coating can be attributed to its low critical load (12 N), which leads to the rapid removal of the coating from the substrate in the early stages of the sliding process and causes severe adhesion wear as a result. While the wear depth and wear rate of the Cr-CH₁₅ coating are lower than those of the Cr-CH₅ coating, they are still generally higher than those of the uncoated substrate. According to the XRD analysis results in Fig. 4, the Cr-CH₁₅ coating has a transition phase between Cr crystalline phase and Cr₇C₃ phase. In other words, it lacks a DLC structure and hence fails to produce a solid lubricant effect at the sliding interface. As a result, it has both a lower H/E ratio (0.057) and a higher friction coefficient (0.306), and therefore suffers a poorer wear rate than the bare SKH51 substrate. By contrast, the Cr-CH₂₅ coating consists of stable Cr₇C₃ phase and has a DLC structure with a large number of sp² bonds. As a result, a solid lubricant effect is produced at the contact surface. Moreover, the H/E ratio of the Cr-CH₂₅ coating increases to 0.063 and the friction coefficient reduces to 0.171. Therefore, the wear depth and wear rate of the Cr-CH₂₅ coating are significantly lower than those of the SKH51 substrate. Finally, the Cr-CH₃₅ coating has the highest carbon content of all the coatings (71.6 at.%), together with the lowest friction coefficient (0.048, 0.05, 0.048), wear depth (0.08, 0.15, 0.18 µm) and wear rate (0.34, 0.33, 0.28 × 10⁻⁶ mm³/Nm) under loads of 2, 5 and 8 N, respectively. Compared with the SKH51 substrate, the Cr-CH₃₅ coating therefore reduces the wear rate by around 23, 25 and 28 times, respectively, for normal loads of 2, 5 and 8 N.

The lower friction coefficient, wear depth and wear rate of the coatings prepared with C₂H₂ flow rates greater than 15 sccm can be attributed mainly to a transition of the coating structure to a DLC-like structure with a large number of sp² bonds (Ref 42–44). The sp² bonds have a low shear strength, and hence they fracture and produce a solid lubricant effect at the contact surface during sliding, which reduces the friction coefficient and wear rate. However, the effects of hydrogen on the tribological properties of the coatings should also be considered. For example, Neuville et al. (Ref 45) indicated that hydrogen atoms fill the dangling bonds on the DLC surface and promote the transformation of sp² bonding to sp³ bonding; thereby rendering the coating structure more stable and resistant to chemical change. Tillmann et al. (Ref 46) compared the friction coefficients of DLC without hydrogen (a-C) and with

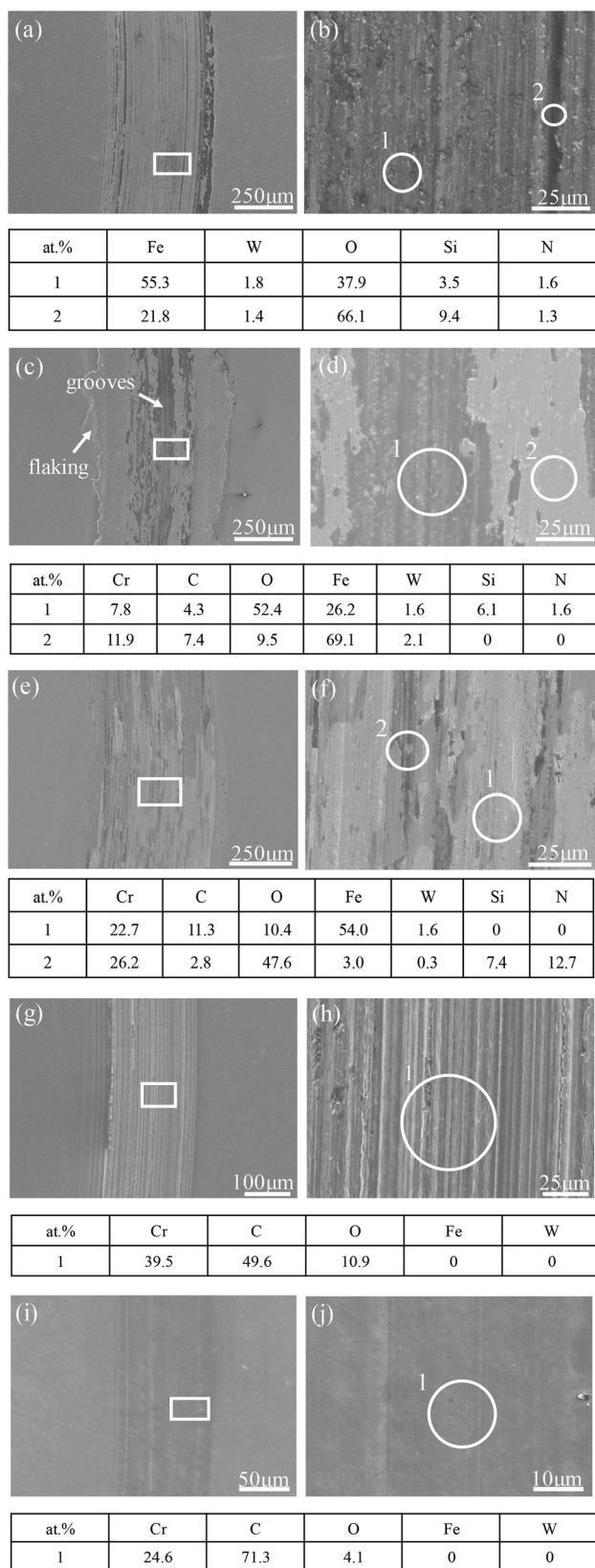


Fig. 14 SEM images and EDS analysis results for wear tracks on (a) SKH51 substrate, (c) Cr-CH₅ coating, (e) Cr-CH₁₅ coating, (g) Cr-CH₂₅ coating, and (i) Cr-CH₃₅ coating. Figures (b), (d), (f), (h) and (j) present enlarged views of square regions indicated in Figures (a), (c), (e), (g) and (i), respectively. (Note that the load is 5 N in every case.)

hydrogen (a-C:H), respectively, in a vacuum environment. It was shown that the presence of hydrogen reduced the friction coefficient from 0.1 (a-C) to 0.05 (a-C:H). It was speculated that the lower friction coefficient was a result of the hydrogen atoms constantly filling the vacancies of the dangling bonds on the surface; hence producing a low-shear-strength polymer-like layer which provided a solid lubricant effect. Vengudusamy et al. (Ref 47) examined the effect of the hydrogen and tungsten concentration on the wear properties of DLC. The results showed that the wear rate of an a-C:H coating in base oil was lower than that of an a-C:H:W coating. Moreover, the wear rate and friction coefficient of the a-C:H coating decreased with an increasing H content.

Notably, the results presented in Figures 11, 12 and 13 confirm that the Cr-CH₃₅ coating with the highest H/E ratio (0.084) of all the coatings has the optimum tribological properties, as predicted in Sect. 3.2.

3.3.2 Wear Mechanisms of Substrate and Coatings. Figure 14 presents SEM images and EDS analysis results for the wear tracks on the uncoated and coated substrates following the sliding tests performed under a normal load of 5 N. (Note that similar results were observed for wear loads of 2 N and 8 N, respectively, and hence the corresponding images are deliberately omitted here.) Figure 14(a) and (b) shows the wear surface and EDS results for the uncoated SKH51 substrate. It is seen that the surface contains a large number of deep scratches. Region 1 of the surface (corresponding to lower-depth wear scratches) has a high iron and oxygen content of 55.3 at.% and 37.9 at.%, respectively, together with a small amount of tungsten (W: 1.8 at.%), silicon (Si: 3.5 at.%) and nitrogen (N: 1.6 at.%). Similarly, region 2 of the surface (corresponding to higher-depth wear scratches) contains 21.8 at.% Fe, 66.1 at.% O and a small amount of tungsten (W: 1.4 at.%), silicon (Si: 9.4 at.%) and nitrogen (N: 1.3 at.%). In other words, the surface of the wear track shows evidence of significant oxidation and material transfer from the Si₃N₄ counterbody during the sliding test. As shown in Fig. 10, the friction coefficient of the SKH51 substrate increases dramatically during the initial sliding stage (approximately 100 cycles) and then continues to rise rapidly to a value of approximately 0.4 after 3300 cycles. However, following this initial running-in period, the friction coefficient remains approximately constant until the end of the wear test. Overall, it is concluded that the wear mechanism of the uncoated SKH51 substrate is one of mixed oxidation and adhesion.

As shown in Fig. 14(c), the Cr-CH₅ coating is severely damaged and contains deep plowing grooves and extensive flaking. Moreover, the EDS analysis results show that region 1 of the wear surface has a significant oxygen and iron content (O: 52.4 at.% and Fe: 26.2 at.%, respectively), together with a small quantity of silicon (Si: 6.1 at.%), tungsten (W: 1.8 at.%) and nitrogen (N: 1.6 at.%) (see Fig. 14d). In other words, the central region of the wear track undergoes oxidation and material transfer from the Si₃N₄ counterbody during the sliding test. In region 2 of the wear track, the surface composition is close to that of the SKH51 substrate (Fe: 69.1 at.%). Moreover, the wear depth (2.22 μm, see Fig. 12) is greater than the coating thickness (2.16 μm, see Fig. 8). Hence, it is inferred that the coating is almost completely destroyed and the wear scar penetrates through the coating and into the underlying substrate. In other words, the Cr-CH₅ coating exhibits a mixed wear mode of abrasion, adhesion and oxidation.

The SEM and EDS analysis results presented in Fig. 14(e) and (f) show that region 1 of the wear track on the Cr-CH₁₅ coating (i.e., the gray regions of the wear track) has a high iron content of Fe: 54.0 at.%. Moreover, region 2 of the wear track (i.e., the black regions of the wear track) has a high oxygen content (O: 47.6 at.%) and a small amount of silicon (Si: 7.4 at.%) and nitrogen (N: 12.7 at.%). Thus, the EDS analysis results suggest that the coating undergoes mixed oxidation and adhesive wear during the sliding test. As shown in Fig. 10, the adhesive wear causes severe oscillations of the friction coefficient and leads to a high wear depth and wear rate as a result (see Figs. 12 and 13, respectively).

Figure 14(g) and (h) presents SEM images and EDS analysis results for the wear track on the Cr-CH₂₅ coating. Although the wear surface contains a large number of scratches, there is no obvious evidence of any debris or adhered material. According to the EDS analysis results, region 1 of the wear surface consists mainly of chromium (Cr: 39.5 at.%) and carbon (C: 49.6 at.%). The composition of the wear surface is thus close to that of the original coating (Cr: 42.5 at.%, C: 52.4 at.%, see Fig. 3), and hence it is inferred that the coating remains largely intact following the sliding wear test. As a result, the friction coefficient of the Cr-CH₂₅ coating has a low and stable value compared to that of the Cr-CH₅ and Cr-CH₁₅ coatings (see Fig. 10). Overall, the results indicate that the Cr-CH₂₅ coating experiences only minor abrasive wear during the wear process and hence suffers only a low wear depth and wear rate, as shown in Figs. 12 and 13.

Figure 14(i) and (j) shows SEM images and EDS analysis results for the wear track on the Cr-CH₃₅ coating. The SEM images show that the wear track contains only minor scratch marks. Moreover, the EDS results show that the elemental composition of the wear track (Cr: 24.6 at.% and C: 71.3 at.%) is almost identical to that of the original coating surface (see Fig. 3). In other words, the coating remains almost entirely intact following the wear test and suffers only minor abrasive wear. As a result, the friction coefficient has an extremely low and stable value (see Fig. 10), and the wear depth and wear rate are the lowest of all the coatings accordingly.

4. Conclusion

Cr-CH_x coatings have been deposited on SKH51 substrates by radio frequency magnetron sputtering with various acetylene fluxes in the range of $x = 5\text{--}35$ sccm. The crystalline structures and mechanical and tribological properties of the coatings have been investigated and compared. The results have shown that the Cr-CH₅ coating has a low carbon content and consists mainly of Cr (110) and Cr (200) phases. By contrast, the Cr-CH₁₅ coating has a transitional structure between Cr crystalline phase and Cr₇C₃ phase. The Cr-CH₂₅ and Cr-CH₃₅ coatings consist mainly of Cr₇C₃ phase and have DLC-like structures as a result of their high carbon contents (i.e., 52.4 at.% and 71.6 at.%, respectively). The hardness of the Cr-CH_x coatings gradually decreases with an increasing acetylene flux due to the greater carbon content. However, the Cr-CH₁₅, Cr-CH₂₅ and Cr-CH₃₅ coatings all have an adhesion strength higher than 100 N since the higher carbon content induces a solid lubricant effect at the sliding interface, which reduces the lateral force acting on the coating. Among all of the coatings, the Cr-CH₃₅ coating has the lowest wear rate (0.34, 0.33 and 0.28×10^{-6}

mm³/Nm) and wear depth (0.08, 0.15 and 0.18 μm) under normal loads of 2, 5 and 8 N, respectively. Overall, the wear rates of the Cr-CH₃₅ coating are approximately 23, 25 and 28 times lower than those of the uncoated SKH51 substrate under normal loads of 2, 5 and 8 N, respectively. In other words, the Cr-CH₃₅ coating possesses superior tribological properties and thus has significant potential as a protective coating for industrial tools with extended service lives.

Acknowledgment

The authors gratefully acknowledge the financial support provided to this study by the Ministry of Science and Technology of Taiwan under Contract No. MOST 108-2221-E-006-182.

Reference

1. B. Kursuncu, Influence of Cryogenic Heat-Treatment Soaking Period and Temperature on Performance of Sintered Carbide Cutting Tools in Milling of Inconel 718, *Int. J. Refractory Metals Hard Mater.*, 2020, **92**, p 105323.
2. F. Careri, D. Umbrello, K. Essa, M.M. Attallah and S. Imbrogno, The Effect of the Heat Treatments on the tool Wear of Hybrid Additive Manufacturing of IN718, *Wear*, 2021, **470–471**, p 203617.
3. N.A. Özbek, Effects of Cryogenic Treatment Types on the Performance of Coated Tungsten Tools in the Turning of AISI H11 Steel, *J. Mater. Res. Technol.*, 2020, **9**, p 9442–9456.
4. H. Ziegele, C. Rebholz, A.A. Voevodin, A. Leyland, S.L. Rohde and A. Matthews, Studies of the Tribological and Mechanical Properties of Laminated CrC–SiC Coatings Produced by r.f. and d.c. Sputtering Tribology, *International.*, 1997, **30**, p 845–856.
5. S. Sen, Influence of Chromium Carbide Coating on Tribological Performance of Steel, *Mater. Des.*, 2006, **27**, p 85–91.
6. L. Yate, L. Martínez-de-Olcoz, V.I. Ivashchenko, A.V. Pshyk, E. Coy and J. Esteve, Stabilization of Complex Orthorhombic o-Cr₃C₂ Thin Films under High Energetic Growth Conditions: Experiments and Calculations, *J. Alloys Compd.*, 2020, **848**, p 156373.
7. M. Detroye, F. Reniers, C. Buess-Herman and J. Vereecken, Synthesis and Characterisation of Chromium Carbides, *Appl. Surf. Sci.*, 1997, **120**, p 85–93.
8. C. Ziebert, J. Ye, M. Stüber, S. Ulrich, M. Edinger and I. Barzen, Ion Bombardment-induced Nanocrystallization of Magnetron-sputtered Chromium Carbide Thin Films, *Surf. Coat. Technol.*, 2011, **205**, p 4844–4849.
9. B. Xiao, J.D. Xing, J. Feng, Y.F. Li, C.T. Zhou, W. Su, X.J. Xie and Y.H. Chen, Theoretical Study on the Stability and Mechanical Property of Cr₇C₃, *Phys. B*, 2008, **403**, p 2273–2281.
10. W.H. Kao, Y.L. Su and S.H. Yao, Tribological Property and Drilling Application of Ti–C: H and Cr–C: H Coatings on High-speed Steel Substrates, *Vacuum*, 2006, **80**, p 604–614.
11. G.M. Bakić, V. Maksimović, A. Maslarević, M.B. Djukić, B. Rajičić, A. Djordjević, Microstructural Characterization Of WC And CrC Based Coatings Applied By Different Processes. *Metallurgical & Materials Engineering Congress of South-East Europe*. 2015
12. Y.L. Su, T.H. Liu, C.T. Su and T.P. Cho, Effect of Chromium Content on the Dry Machining Performance of Magnetron Sputtered Cr_xC Coatings, *Mater. Sci. Eng.*, 2004, **A346**, p 188–197.
13. C. Pusch, H. Hoche, C. Berger, R. Riedel, E. Ionescu and A. Klein, Influence of the PVD sputtering method on structural characteristics of SiCN-Coatings-Comparison of RF DC and HiPIMS Sputtering and Target Configurations, *Surf. Coat. Technol.*, 2011, **205**, p 119–123.
14. B. Coto, P. Hallander, L. Mendizabal, F. Pagano, H. Kling, R. Ortiz, J. Barriga and L. Selegård, Particle and Rain Erosion Mechanisms on Ti/TiN Multilayer PVD Coatings for Carbon Fibre Reinforced Polymer Substrates Protection, *Wear*, 2021, **466–467**, p 203575.
15. K.B. Sundaram and J. Alizadeh, Deposition and Optical Studies of Silicon Carbide Nitride Thin Films, *Thin Solid Films*, 2000, **370**, p 151–154.

16. J.P. Wang, Y.H. Lu and Y.G. Shen, Effect of Nitrogen Content on Phase Configuration, Nanostructure and Mechanical Behaviors in Magnetron Sputtered SiC_xN_y Thin Films, *Appl. Surf. Sci.*, 2010, **256**, p 1955–1960.
17. S.K. Mishra and A.S. Bhattacharyya, Effect of Substrate Temperature on the Adhesion Properties of Magnetron Sputtered Nano-Composite Si-C-N Hard Thin Films, *Mater. Lett.*, 2008, **62**, p 398–402.
18. A. Baptista, F.J.G. Silvab, J. Porteiro, J.L. Míguez, G. Pinto and L. Fernandes, On the Physical Vapour Deposition (PVD): Evolution of Magnetron Sputtering Processes for Industrial Applications, *Procedia Manufacturing.*, 2018, **17**, p 746–757.
19. A.O.O.A. Esther, O.P. Oladijo and J.D. Majumdar, Surface Integrity of TiC Thin Film Produced by RF Magnetron Sputtering, *Procedia Manufacturing.*, 2019, **35**, p 950–955.
20. S. Özen and V. Şenay, Optical, Morphological and Nano-mechanical Properties of Chromium Oxide Thin Films Fabricated by Radio Frequency (RF) Magnetron Sputtering, *Optik*, 2020, **201**, p 163433.
21. N. Akin, B. Kinaci, Y. Ozen and S. Ozelcik, Influence of RF Power on the Opto-electrical and Structural Properties of Gallium-doped Zinc Oxide Thin Films, *Mater Electron*, 2017, **28**, p 7376–7384.
22. G.M. Wu, A.K. Sahoo and C.Y. Liu, Influence of RF Power on Performance of Sputtered a-IGZO Based Liquid Crystal Cells, *Thin Solid Films*, 2015, **596**, p 56–62.
23. M. Schwartzkopf, A. Hinz, O. Polonskyi, T. Strunskus, F.C. Löhner, V. Körtgens, P. Müller-Buschbaum, F. Faupel and S.V. Roth, Role of Sputter Deposition Rate in Tailoring Nanogranular Gold Structures on Polymer Surfaces, *Appl. Mater. Interfaces.*, 2017, **9**, p 5629–5637.
24. P. Souček, J. Daniel, J. Hnilica, K. Bernátová, L. Zábranský, V. Buršíková, M. Stupavská and P. Vašina, Superhard Nanocomposite nc-TiC/a-C: H Coatings: The Effect of HiPIMSON Coating Microstructure and Mechanical Properties, *Surf. Coat. Technol.*, 2017, **311**, p 257–267.
25. B. Wu, G. Lin, Y. Fu, M. Hou and B. Yi, Chromium-containing Carbon Film on Stainless Steel as Bipolar Plates for Proton Exchange Membrane Fuel Cells, *Int. J. Hydrogen Energy*, 2010, **35**, p 3255–3261.
26. W. Olovsson, B. Alling and M. Magnuson, Structure and Bonding in Amorphous Cr_{1-x}C_x Nanocomposite Thin Films: X-ray Absorption Spectra and First-Principles Calculations, *J. Phys. Chem. C.*, 2016, **120**, p 12890–12899.
27. A.G. Kvashnin, A.R. Oganov, A.I. Samtsevich and Z. Allahyari, Computational Search for Novel Hard Chromium-Based Materials, *J. Phys. Chem. Lett.*, 2017, **8**, p 755–764.
28. D. Music, U. Kreissig, R. Mertens and J.M. Schneider, Electronic Structure and Mechanical Properties of Cr₇C₃, *Phys. Lett. A*, 2004, **326**, p 473–476.
29. M. Andersson, J. Högström, S. Urbonaite, A. Furlan, L. Nyholm and U. Jansson, Deposition and Characterization of Magnetron Sputtered Amorphous Cr-C Films, *Vacuum*, 2012, **86**, p 1408–1416.
30. C. Casiraghi, A.C. Ferrari and J. Robertson, Raman Spectroscopy of Hydrogenated Amorphous Carbons, *Phys. Rev.*, 2005, **72**, p 085401.
31. Y. Gao and P. Yin, Determination of Crystallite size of Nanodiamond by Raman Spectroscopy, *Diamond Related Mater.*, 2019, **99**, p 107524.
32. W. Dai, H. Zheng, G. Wu and A. Wang, Effect of Bias Voltage on Growth Property of Cr-DLC Film Prepared by Linear Ion Beam Deposition Technique, *Vacuum*, 2010, **85**, p 231–235.
33. S. Praver, K.W. Nugent, Y. Lifshitz, G.D. Lempert, E. Grossman, J. Kulik, I. Avigal and R. Kalish, Systematic Variation of the Raman Spectra of DLC Films as a Function of sp²: sp³ Composition, *Diam. Relat. Mater.*, 1996, **5**, p 433–438.
34. A.C. Ferrari and J. Robertson, Interpretation of Raman Spectra of Disordered and Amorphous Carbon, *Phys. Rev.*, 2000, **61**, p 14095.
35. S. Piscanec, F. Mauri, A.C. Ferrari, M. Lazzeri and J. Robertson, Ab Initio Resonant Raman Spectra of Diamond-like Carbons, *Diam. Relat. Mater.*, 2005, **14**, p 1078–1083.
36. B. Ren, Z.X. Liu, L. Shi, B. Cai and M.X. Wang, Structure and Properties of (AlCrMnMoNiZrB_{0.1})_{N_x} Coatings Prepared by Reactive DC Sputtering, *Appl. Surf. Sci.*, 2011, **257**, p 7172–7178.
37. Y.L. Su, T.H. Liu, C.T. Su and T.P. Cho, Effect of Chromium Content on the dry Machining Performance of Magnetron Sputtered Cr_xC Coatings, *Mater. Sci. Eng., A*, 2004, **364**, p 188–197.
38. Y.S. Jhong, C.W. Huang and S.J. Lin, Effects of CH₄ Flow Ratio on the Structure and Properties of Reactively Sputtered (CrNbSiTiZr)C_x Coatings, *Mater. Chem. Phys.*, 2018, **210**, p 348–352.
39. I. Hutchings and P. Shipway, *Tribology: Friction and Wear of Engineering Materials*, Butterworth-Heinemann, US, 2017
40. A. Leyland and A. Matthews, On the Significance of the H/E Ratio in Wear Control: A Nanocomposite Coating Approach to Optimised Tribological Behavior, *Wear*, 2000, **245**, p 1–11.
41. J. Guo, H. Wang, F. Meng, X. Liu and F. Huang, Tuning the H/E* Ratio and E* of AlN Coatings by Copper Addition, *Surf. Coat. Technol.*, 2013, **228**, p 68–75.
42. L. Wu, X. Guo and J. Zhang, Abrasive Resistant Coatings—A Review, *Lubricants*, 2014, **2**, p 66–89.
43. F.-D. Duminica, R. Belchi, L. Libralesso and D. Mercier, Investigation of Cr(N)/DLC Multilayer Coatings Elaborated by PVD for High Wear Resistance and Low Friction Applications, *Surf. Coat. Technol.*, 2018, **337**, p 396–403.
44. L. Huang, J. Yuan, C. Li and D. Hong, Microstructure, Tribological and Cutting Performance of Ti-DLC/α-C: H Multilayer Film on Cemented Carbide, *Surf. Coat. Technol.*, 2018, **353**, p 163–170.
45. S. Neuville and A. Matthews, A Perspective on the Optimisation of Hard Carbon and Related Coatings for Engineering Applications, *Thin Solid Films*, 2007, **515**, p 6619–6653.
46. W. Tillmann, E. Vogli and F. Hoffmann, Wear-resistant and Low-friction Diamond-Like-Carbon (DLC)-Layers for Industrial Tribological Applications under Humid Conditions, *Surf. Coat. Technol.*, 2009, **204**, p 1040–1045.
47. B. Vengudusamy, J.H. Green, G.D. Lamb and H.A. Spikes, Influence of Hydrogen and Tungsten Concentration on the Tribological Properties of DLC/DLC Contacts with ZDDP, *Wear*, 2013, **298–299**, p 109–119.

Publisher's Note Springer Nature remains neutral with regard to jurisdictional claims in published maps and institutional affiliations.